The Astrophysical Journal, 727:101 (11pp), 2011 February 1 doi:10.1088/0004-637X/727/2/101

RECONSTRUCTION OF THE CORONAL MAGNETIC FIELD USING THE CESE–MHD METHOD

Chaowei Jiang[1,2], Xueshang Feng[1], Yuliang Fan[3,4], and Changqing Xiang[1]
[1] SIGMA Weather Group, State Key Laboratory for Space Weather, Center for Space Science and Applied Research, Chinese Academy of Sciences, Beijing 100190, China; cwjiang@spaceweather.ac.cn, fengx@spaceweather.ac.cn, cqxiang@spaceweather.ac.cn
[2] College of Earth Sciences, Graduate University of Chinese Academy of Sciences, Beijing 100049, China
[3] Key Laboratory of Solar Activity, National Astronomical Observatories, Chinese Academy of Sciences, Beijing 100012, China; fanyuliang@bao.ac.cn
[4] College of Physics, Graduate University of Chinese Academy of Sciences, Beijing 100049, China
Received 2010 October 13; accepted 2010 November 17; published 2011 January 10

ABSTRACT

We present a new implementation of the MHD relaxation method for reconstruction of the nearly force-free coronal magnetic field from a photospheric vector magnetogram. A new numerical MHD scheme is proposed to solve the full MHD equations by using the spacetime conservation-element and solution-element method. The bottom boundary condition is prescribed in a similar way as in the stress-and-relax method, by changing the transverse field incrementally to match the magnetogram, and other boundaries of the computational box are set by the nonreflecting boundary conditions. Applications to the well-known benchmarks for nonlinear force-free-field reconstruction, the Low & Lou force-free equilibria, validate the method and confirm its capability for future practical application, with observed magnetograms as inputs.

Key words: magnetic fields – magnetohydrodynamics (MHD) – methods: numerical – Sun: corona

1. INTRODUCTION

It is commonly believed that the magnetic field plays an important role in active solar phenomena: solar flares, coronal mass ejections, and other solar eruptive activities (Priest & Forbes 2002). The knowledge of three-dimensional (3D) magnetic-field properties is essential for our understanding of the physical mechanism of these activities. Unfortunately, the direct measurement of the 3D magnetic field in higher solar atmospheres is far less precise and sophisticated than in the photosphere. The currently most common and accurate way of overcoming this is to extrapolate the magnetic field into the solar chromosphere and corona, based on an assumed model and using the observed photospheric magnetic field as a boundary condition. There have been several techniques developed for the extrapolation of the magnetic field for this purpose, and most of them adopt the force-free-field model (McClymont et al. 1997; Schrijver et al. 2006; Wiegelmann 2008). This is a good approximation for the low corona, because the magnetic field is nearly force-free in most parts of active regions (Metcalf et al. 1995) because of low plasma β ($\beta = 2\mu_0 p/B^2 \ll 1$) and low plasma velocity $v \ll v_A$ (Alfvén speed) there, which means that the pressure gradient, gravity, and inertial force can be neglected.

The force-free field can be described by the equations

$$\nabla \times \mathbf{B} = \alpha \mathbf{B}, \qquad \nabla \cdot \mathbf{B} = 0, \tag{1}$$

where $\mathbf{B}$ is the magnetic field and α, usually called the force-free parameter, is a scalar function of space. From Equation (1), one derives $\mathbf{B} \cdot \nabla\alpha = 0$; consequently, in the force-free field, α is constant along each individual field line but can have different values on different field lines. If the force-free parameter α is constant for all field lines, then Equation (1) is linear and we are dealing with linear, force-free extrapolation. Particularly, the force-free parameter $\alpha = 0$ yields a potential field, with no extra free energy contained to energize eruptive solar activity. Also, the linear method is inadequate because of its limitation on the match of most observed magnetograms, because in observations the force-free parameter α is greatly changed across active regions (Régnier et al. 2002). It is necessary to go beyond the linear method and utilize the nonlinear approximation.

Nonlinear extrapolation methods can be generally categorized into iterative methods and evolutionary methods (Valori et al. 2005). The iterative methods iterate equations to get the best approximate solutions of Equation (1). One example of iterative methods is the boundary-integral-equation (BIE) method, first proposed by Yan & Sakurai (2000) and improved by Yan & Li (2006), who proposed it as the direct-boundary-integral-equation (DBIE) formulation. Recently, He & Wang (2008) followed the main idea of DBIE and devised the upward-boundary-integration scheme. This method represents the force-free magnetic field by direct integration of the magnetic field with the bottom boundary. Other important iterative methods can be found in Wiegelmann (2008).

The evolutionary methods or the magnetohydrodynamics (MHD)-relaxation methods (Yang et al. 1986; Mikic & McClymont 1994; McClymont & Mikic 1994; Roumeliotis 1996; McClymont et al. 1997) usually use a potential field as the initial field and evolve this field into a nonlinear force-free field (NLFFF). These methods follow the time evolution of the resistive, viscous, MHD equations and allow the boundary conditions to change to match the observed magnetogram. In the method implemented by Mikic & McClymont (1994), specifically, a subset of the full MHD equations, the so-called zero-beta model

$$\begin{aligned} \rho \frac{D\mathbf{v}}{Dt} &= \mathbf{J} \times \mathbf{B} + \nabla \cdot (\nu\rho\nabla\mathbf{v}), \\ \frac{\partial \mathbf{A}}{\partial t} &= \mathbf{v} \times \mathbf{B} - \eta \mathbf{J} \end{aligned} \tag{2}$$

is solved. Here, $\mathbf{J} = \nabla \times \mathbf{B}$, $\mathbf{B} = \nabla \times \mathbf{A}$, and the density ρ may be fixed as a constant or set as $\rho \propto B^2$ for a uniform Alfvén speed to accelerate the evolution of the weak field. The bottom boundary condition is applied to the magnetic flux B_z and the transverse electric field $\mathbf{E}_t$. The former is adopted from the magnetogram directly, while the latter is specified in a rather indirect and complicated way (but possibly suitable for their code). That is, the electric field $\mathbf{E}_t$ is artificially made to vary in such a manner that it can continually drive the normal-current density, j_z, on the boundary toward the desired distribution (deduced from the magnetogram), and at the same time not alter the

magnetic flux B_z, according to the normal induction equation $\frac{\partial B_z}{\partial t} = -\nabla \times \mathbf{E}_t$. Eventually, the field approaches the force-free state, with the bottom boundary matching B_z and $j_z$from the magnetogram. It should be noted that the normal electric-current density j_z is once again indirectly determined from the magnetogram by taking finite differences in the transverse field and may be unreliable at many locations, because the measured transverse field already has large errors (Roumeliotis 1996).

Roumeliotis (1996) introduced another similar evolutionary method, the so-called stress-and-relax method, which also uses the same subset of the MHD equations (2) to obtain the final asymptotic equilibrium, but with simplifications of the momentum equation (using the magnetofrictional assumption, given below) and the boundary conditions. A new implementation of the stress-and-relax method was proposed by Valori et al. (2005), also called the magnetofrictional method, which directly used the magnetic-induction-field vector **B** instead of the vector potential **A** and utilized an existing MHD code, the Versatile Advection Code (VAC; Tóth 1996). In this kind of method, the dissipative term $\mathbf{D}(\mathbf{v})$ in the momentum equation

$$\rho \frac{D\mathbf{v}}{Dt} = \mathbf{J} \times \mathbf{B} + \mathbf{D}(\mathbf{v}) \tag{3}$$

for relaxation of the system is chosen to be a friction-like force, as $\mathbf{D}(\mathbf{v}) = -\nu\mathbf{v}$ (Yang et al. 1986), where ν is a properly given function of space and time that optimizes relaxation progress. Then, the momentum equation is further reduced to

$$\mathbf{v} = \frac{1}{\nu}\mathbf{J} \times \mathbf{B} \tag{4}$$

by neglecting the inertial term, and thus the only equation that needs to be solved is the induction equation. The bottom boundary condition is applied by simply changing the transverse field incrementally (or in a single-step way) to match the magnetogram. In such a process, the Lorentz force is injected from the bottom and stresses the system away from the initial potential field, and relaxation after the stress step takes the system to a new equilibrium. An improved implementation of the magnetofrictional method by Valori et al. (2007) was used in the reconstruction of force-free equilibria by Low & Lou (1990). Recently, Valori et al. (2010) extended their code to the reconstruction of the flux-rope equilibrium from Titov & Démoulin (1999).

The above methods were all designed for the purpose of obtaining an "exact" solution to the NLFFF; however, one should always bear in mind that the force-free field is only an approximation of the real coronal field, and the "exact" force-free coronal field does not exist. In this paper, in order to reconstruct the coronal field in a more general and realistic condition, we return to the full MHD system (including the gas pressure and the viscous and resistive terms) to implement the MHD-relaxation method in a more natural way. The nonzero pressure is included via a simple adiabatic model of the low-corona atmosphere, with low $\beta(\leqslant 0.01)$ to mimic the realistic coronal condition. Modeling such a low β plasma by the full MHD is a challenge for numerical methods (e.g., a negative pressure unacceptable for the real physical situation may arise in many methods; Balsara & Spicer 1999), and this seems to be one of the reasons for totally discarding the pressure term in the above-mentioned relaxation methods. Here, a novel high-resolution and high-performance numerical scheme, the spacetime conservation-element and solution-element (CESE) method, is used for solving the full MHD equations (Zhang et al. 2006; Feng et al. 2006, 2007, 2009, 2010). This method is most suitable for the full set of the governing equations written in the form of conservation laws, because it differs greatly from the traditional numerical methods by treating space and time as one entity. It has a solid foundation in physics and yet offers simple mathematics and coding. The bottom boundary condition is given in a similar way as in the stress-and-relax method, and the other faces of the modeling domain are set to be nonreflecting. As a first validation of the model, the force-free equilibria of Low & Lou (1990) will be reconstructed.

The content of the paper is as follows. In Section 2, the method and its numerical implementation are briefly given. In Section 3, applications to the extrapolation of Low & Lou (1990)'s test cases are reported and analyzed. Finally, we summarize and give some projections for the method in Section 4.

2. THE METHOD

2.1. The CESE–MHD Model

We solve a full system of the MHD model by the CESE method. The basic governing equations are written in a standard conservation form, with source terms as follows:

$$\frac{\partial \mathbf{U}}{\partial t} + \frac{\partial \mathbf{F}}{\partial x} + \frac{\partial \mathbf{G}}{\partial y} + \frac{\partial \mathbf{H}}{\partial z} - \frac{\partial \mathbf{F}_v}{\partial x} - \frac{\partial \mathbf{G}_v}{\partial y} - \frac{\partial \mathbf{H}_v}{\partial z} = \mathbf{S}, \tag{5}$$

where

$$\mathbf{U} = (\rho, \rho\mathbf{v}, p, \mathbf{B}) = (\rho, \rho v_x, \rho v_y, \rho v_z, p, B_x, B_y, B_z)^T, \tag{6}$$

$$\mathbf{F} = \begin{pmatrix} \rho v_x \\ \rho v_x^2 + p_0 - B_x^2 \\ \rho v_x v_y - B_x B_y \\ \rho v_x v_z - B_x B_z \\ \gamma p v_x \\ 0 \\ v_x B_y - v_y B_x \\ v_x B_z - v_z B_x \end{pmatrix}; \mathbf{G} = \begin{pmatrix} \rho v_y \\ \rho v_y v_x - B_y B_x \\ \rho v_y^2 + p_0 - B_y^2 \\ \rho v_y v_z - B_y B_z \\ \gamma p v_y \\ v_y B_x - v_x B_y \\ 0 \\ v_y B_z - v_z B_y \end{pmatrix};$$

$$\mathbf{H} = \begin{pmatrix} \rho v_z \\ \rho v_z v_x - B_z B_x \\ \rho v_z v_y - B_z B_y \\ \rho v_z^2 + p_0 - B_z^2 \\ \gamma p v_z \\ v_z B_x - v_x B_z \\ v_z B_y - v_y B_z \\ 0 \end{pmatrix}, \tag{7}$$

$$\mathbf{F}_v = \begin{pmatrix} 0 \\ \nu\rho\frac{\partial v_x}{\partial x} \\ \nu\rho\frac{\partial v_y}{\partial x} \\ \nu\rho\frac{\partial v_z}{\partial x} \\ 0 \\ \mu\nabla\cdot\mathbf{B} \\ \eta j_z \\ -\eta j_y \end{pmatrix}; \mathbf{G}_v = \begin{pmatrix} 0 \\ \nu\rho\frac{\partial v_x}{\partial y} \\ \nu\rho\frac{\partial v_y}{\partial y} \\ \nu\rho\frac{\partial v_z}{\partial y} \\ 0 \\ -\eta j_z \\ \mu\nabla\cdot\mathbf{B} \\ \eta j_x \end{pmatrix}; \mathbf{H}_v = \begin{pmatrix} 0 \\ \nu\rho\frac{\partial v_x}{\partial z} \\ \nu\rho\frac{\partial v_y}{\partial z} \\ \nu\rho\frac{\partial v_z}{\partial z} \\ 0 \\ \eta j_y \\ -\eta j_x \\ \mu\nabla\cdot\mathbf{B} \end{pmatrix}, \text{ and} \tag{8}$$

Table 1
Reference Values for Nondimensionalization

Quantity	Reference	Value
$\mathbf{r}$	L_0	100 Mm
$\mathbf{B}$	B_0	10 G
ρ	$\rho_0 = 1 \times 10^9$ cm$^{-3} m_p$	1.672×10^{-15} cm^{-3} g
$\mathbf{v}$	$v_A = B_0/\sqrt{\mu_0 \rho_0}$	690 km s^{-1}
t	$\tau_A = L_0/v_A$	2.4 minutes
p	$p_0 = B_0^2/\mu_0$	0.8 Pa
$\mathbf{j}$	$j_0 = B_0/(\mu_0 L_0)$	8×10^{-4} A
ν	$L_0 v_A$	69 Mm^2 s^{-1}
η	$\mu_0 L_0 v_A$	87 Ω Mm

Note. Here, μ_0 is the permeability of a vacuum, m_p is the proton mass, v_A is the Alfvén speed, and τ_A is the Alfvén time. 1 Mm $= 1 \times 10^6$ m.

$$\mathbf{S} = [0, \rho\mathbf{g}, (\gamma - 1)\mathbf{v} \cdot \nabla p + H, \mathbf{0}]^T - \nabla \cdot \mathbf{B}\,(0, \mathbf{B}, 0, \mathbf{v})^T\,, \quad (9)$$

with the total pressure $p_0 = p + (B_x^2 + B_y^2 + B_z^2)/2$. Here, ρ, $\mathbf{v}$, p, and $\mathbf{B}$ are the mass density, plasma velocity, gas pressure, and magnetic field, respectively. (j_x, j_y, j_z) are the components of the electric current $\mathbf{J}$. ν is the kinematic plasma viscosity and η is the electrical resistivity. γ is the ratio of the specific heats with a value of $\gamma = 1.05$, which is usually employed to simply describe the thermodynamics in the lower corona instead of using other complicated coronal-heating terms (Mikić & Linker 1994; Mikić et al. 1999; Hu et al. 2008). $\mathbf{r}$ is the position vector and t is time. The gravity $\mathbf{g}$ is a function of z given by

$$\mathbf{g}(z) = -g_0 \frac{R_\odot^2}{(R_\odot + z)^2} \mathbf{e_z}, \quad (10)$$

where $R_\odot$ is the solar radius and $g_0 = 274$ m s^{-2} is the surface gravity. The heating term from resistivity and viscosity, $H = (\gamma - 1)(\eta \mathbf{j} \cdot \mathbf{j} + \nu\rho \nabla \mathbf{v} \colon \nabla \mathbf{v})$, is neglected to describe a simple adiabatic process (Mikić & Linker 1994; Amari et al. 2003). Such an assumption is reasonable because of the low values used for the dissipation coefficients η, ν (given below), and because the evolution of the magnetic field is insensitive to this heating term.

At the same time, Powell's source terms $-\nabla \cdot \mathbf{B}(0, \mathbf{B}, 0, \mathbf{v})^T$ are added to deal with the divergence of the magnetic field (Powell et al. 1999). These terms can advect the magnetic monopoles (i.e., the error of $\nabla \cdot \mathbf{B}$) with the velocity of the plasma, and such advection is interpreted as a magnetic-flux wave in addition to the seven existing wave modes (i.e., an entropy wave, a pair of Alfvén waves, and two pairs of magneto-acoustic waves). We also use the diffusive control of $\nabla \cdot \mathbf{B}$ (Marder 1987; Dedner et al. 2002; Tóth et al. 2006) by adding the term $\mu \nabla \cdot \mathbf{B}$ to viscous fluxes $\mathbf{F}_v$, $\mathbf{G}_v$, $\mathbf{H}_v$, which is equivalent to adding a diffusive source term $\nabla(\mu \nabla \cdot \mathbf{B})$ to the magnetic-induction equation.

The primitive variables ρ, $\mathbf{v}$, p, $\mathbf{B}$, current density $\mathbf{j}$, position vector $\mathbf{r}$, time t, viscosity ν, and resistivity η in Equation (5) have been nondimensionalized by their corresponding reference values given in Table 1.

The CESE method deals with the 3D governing equations in a substantially different but general way from the traditional finite-difference or finite-volume methods. It first defines a four-dimensional (4D) Euclidean space E_4, with (x, y, z) as the first three coordinates $(x_1, x_2, x_3) = (x, y, z)$ and time as the fourth one, $x_4 = t$. Using Gauss' divergence theorem in E_4 with the governing equation (5) gives

$$\oint_{S(V)} \mathbf{h}_m \cdot d\mathbf{s} = \int_V S_m dV, \quad (m = 1, 2, 3, \ldots, 8), \quad (11)$$

where $\mathbf{h}_m = (F_m - F_{vm}, G_m - G_{vm}, H_m - H_{vm}, U_m)$ is the spacetime flux vector, $S(V)$ is the boundary of the spacetime region V in E_4, and $\mathbf{h}_m \cdot d\mathbf{s}$ is the spacetime flux exiting through the surface element $d\mathbf{s}$. Then, the 3D solution volume and time form a 4D solution volume in the space E_4, and this 4D solution volume is divided into non-overlapping volume elements that are called conservation elements (CEs). Moreover, the solution elements (SEs) consist of the hyperplanes immediately associated with the solution point and are introduced to relate the spacetime flux values on the hypersurfaces of the CEs with the discretized variables on the solution points. The relationship is carried out by the first-order Taylor expansion because the discretized variables contain the first-order spatial derivatives of U_m, i.e., U_{mx}, U_{my}, and U_{mz}. Applying the spacetime flux conservation of Equation (11) to the CEs results in simple linear relationships of the solution variables (the discretized variables) at two time levels, and the solution is advanced by these relationships. Detailed derivations and descriptions of the method for different dimensions can be found in the references cited in Section 1, especially those for the MHD (Feng et al. 2006, 2007; Jiang et al. 2010).

In addition to Powell's eight-wave scheme (Powell et al. 1999) and the diffusive-control approach, the Poisson projection method is also adopted to further eliminate the numerical error in $\nabla \cdot \mathbf{B}$. Specifically, when it is necessary (i.e., the numerical $\nabla \cdot \mathbf{B}$ reaches a given threshold), we solve the Poisson equation $\nabla^2 \phi = \nabla \cdot \mathbf{B}$ and project the magnetic field to the divergence-free solution $\mathbf{B}' = \mathbf{B} - \nabla\phi$ after each advancing time step. The bi-conjugate gradient-stabilized (Bi-CGSTAB) method, which is a Krylov subspace-type iterative solver, is used to solve the Poisson equation (Van der Vorst 1992; Tóth 2000).

As is usually done for modeling the local magnetic field, the computational domain is represented by a 3D rectangular box in Cartesian coordinates with the bottom boundary on the solar surface, which is in the x–y plane in our coordinate systems. For spatial discretization, we use a mesh that is uniform in the x–y plane, with grid size $\Delta x = \Delta y$, and non-uniform in the z-direction, with grids concentrated near the bottom and increasing gradually upward. Moreover, the computational domain is made moderately larger than the central region of the field to reduce the side-and-top boundary effects (which are reduced further by adopting the nonreflecting boundary conditions (NRBCs) as described in Section 2.3). Because the magnetic field decreases much more slowly in high altitudes than in low altitudes, using this non-uniform and half-adaptive mesh can save significant computational resources without significantly affecting computational accuracy compared with a mesh uniform in all directions.

Finally, choosing a proper viscosity is particularly important. If the viscosity is too strong, the system is difficult to drive, and the relaxation will cost too much CPU time due to not only the limited velocity but also the time step restricted by the Courant–Friedrichs–Lewy (CFL) condition:

$$\Delta t < 0.5 \frac{\Delta x^2}{\nu}. \quad (12)$$

A viscosity that is too small, on the other hand, will lead to a velocity that is too large ($\geqslant v_A$), which may distort the

field line excessively, change the density profile and pressure of the plasma significantly, and, even worse, bring numerical instability to the simulation. For a compromise, we set $\nu = 0.4\Delta x^2/\Delta t$, where Δt is determined only by the maximum Alfvén speed $B/\sqrt{\rho}$ in the domain with the CFL condition. In this way, we maximize viscosity without decreasing the time step. Note that the viscosity is time and space dependent according to the variables Δx and Δt, and the same value is used for the coefficient μ in the diffusive term of $\nabla \cdot \mathbf{B}$. In the present tests, the resistive term is neglected for modeling the ideal MHD by setting $\eta = 0$.

2.2. Initial Conditions

The computation is initialized with a potential magnetic field and an isothermal plasma in hydrostatic equilibrium in the solar gravitational field. The potential field is obtained by solving Laplace's equation $\nabla^2\phi = 0$ with the bottom boundary condition given by the normal component of the vector magnetogram, $\frac{\partial\phi}{\partial z} = B_z$. Laplace's equation is represented by a large sparse system of linear equations after being discretized on the grid using a finite difference. These equations are solved by the same Bi-CGSTAB method that is suitable and efficient for such large, sparse linear systems. In this way, the derived field $\mathbf{B} = \nabla\phi$ will fully match the given boundary map, and the information contained in the map will be preserved. This is unlike Green's function method or other eigenfunction expansion methods that will alter the boundary map because of truncation terms. To approximate the low β condition, the plasma is described by the typical values in the low corona, and the maximum magnetic field on the bottom is set to be $\sim$100 G, which is also a typical value. The plasma density on the bottom ρ_0 is assumed to be uniform, with the proton number density given by $n_0 = 1 \times 10^9$ cm^{-3} and the initial temperature set to be $T = 0.5 \times 10^6$ K. In a hydrostatic equilibrium, the density is

$$\rho(x, y, z) = \rho_0 \exp\left[-z \Big/ \left(\frac{RT(R_\odot + z)}{g_0 R_\odot}\right)\right], \qquad (13)$$

where R is the gas constant of the plasma and the pressure is given by $p = \rho RT$. The leading reason for choosing such a configuration is to maintain the low β condition for the central region of the computational domain.

2.3. Boundary Conditions

As emphasized by Schrijver et al. (2006), implementation of the boundary conditions is the most important limitation to successful field extrapolation. In reality, the field is infinite, while in the numerical models it is only partly represented in a finite volume. Thus, a truly "correct" boundary condition should be characterized by the real field values on the boundary face. Specifically, in addition to the bottom face, the real vector field should be used as the boundary condition at the lateral and top faces (and it is such boundary conditions that make the best results reported in Schrijver et al. 2006). However, this information is not available for real magnetograms. For such case, the so-called NRBCs are frequently used to produce solutions with the desired behavior (Hedstrom 1979; Thompson 1987; Wu et al. 2001). The NRBCs are designed such that flow disturbances can propagate out from the computational volume smoothly without inducing substantial spurious reflections from the boundary.

In the present work, the lateral and top faces are set by the NRBCs to minimize the boundary effects for our consideration. A linear extrapolation may have the nonreflecting effect in some simple cases (e.g., Valori et al. 2005) but always results in instability and even crashes in our practice of the full MHD simulation. In order to implement this type of boundary condition in a more theory-based or reliable way, we use the method of projected characteristics, which was originated by Nakagawa (1981) and implemented by Wu & Wang (1987), and has been used in dealing with the sub-Alfvénic boundary of the Extreme-Ultraviolet Imaging Telescope wave simulation, the data-driven modeling of active-region evolution, and, recently, the solar corona–solar wind modeling (Wu et al. 2001, 2006, 2009; Hayashi 2005; Hayashi et al. 2006, 2008). The basic concept of the projected-characteristics method can be described as follows: (1) the hyperbolic system can be eigendecomposed into a set of wave equations (i.e., compatibility equations), each of which specifies one basic wave mode with the path of the wave called the characteristic; (2) projected in the normal direction of the boundary, there are waves propagating in and out of the computational domain because the wave speeds (the eigenvalues) of both signs generally exist at the boundary; and (3) the NRBCs allow the outgoing waves to go through the boundary surface freely without reflection, and no disturbance will be generated on the surface to affect the interior of the computational domain, which means no incoming waves will come from outside. In practice, the compatibility equations related to the outgoing waves need to be used when updating the boundary quantities. The incoming waves are eliminated by keeping their amplitudes constant, as it is the change in amplitude that indicates a wave. Detailed derivations and formulae of this method are given in Appendix A.

On the bottom boundary, we fix the density and pressure and set the constant velocity $\mathbf{v} = \mathbf{0}$. The normal component of the magnetic field is also unchanged to be identical to the magnetogram. During the time when the field evolves from the initial potential state to the near-force-free state (magnetohydrostatic state in the low β medium), the tangential field is linearly changed from the initial bottom field to the vector magnetogram in tens of Alfvén time τ_A. In this way, the change rate of the tangential magnetic field at the bottom boundary is much slower than the Alfvén speed. By changing the bottom magnetic field, as in the stress-and-relax approach, Lorentz forces are continuously injected into the computational volume to drive the system away from the initial equilibrium. Once the full match of the bottom-vector magnetogram is reached, the boundary is fixed for the system to relax. When the plasma flows generated by the driven force are dissipated sufficiently by the plasma viscosity to a level of $|\mathbf{v}| \ll v_A$, the terms related to velocity $\mathbf{v}$ can be neglected in the momentum equation, after which only the terms of Lorentz force and pressure are left. As provided in the low β condition, the final field is regarded as a force-free state.

3. METHOD VALIDATION

The NLFFF model of Low & Lou (1990), which is a standard benchmark for NLFFF extrapolation codes, is used to validate our method. The fields of this model are basically axially symmetric and can be represented by a second-order partial-differential equation in spherical coordinates

$$(1 - \cos^2\theta)\frac{d^2P}{d(\cos\theta)^2} + n(n+1)P + a^2\frac{1+n}{n}P^{1+2/n} = 0, \quad (14)$$

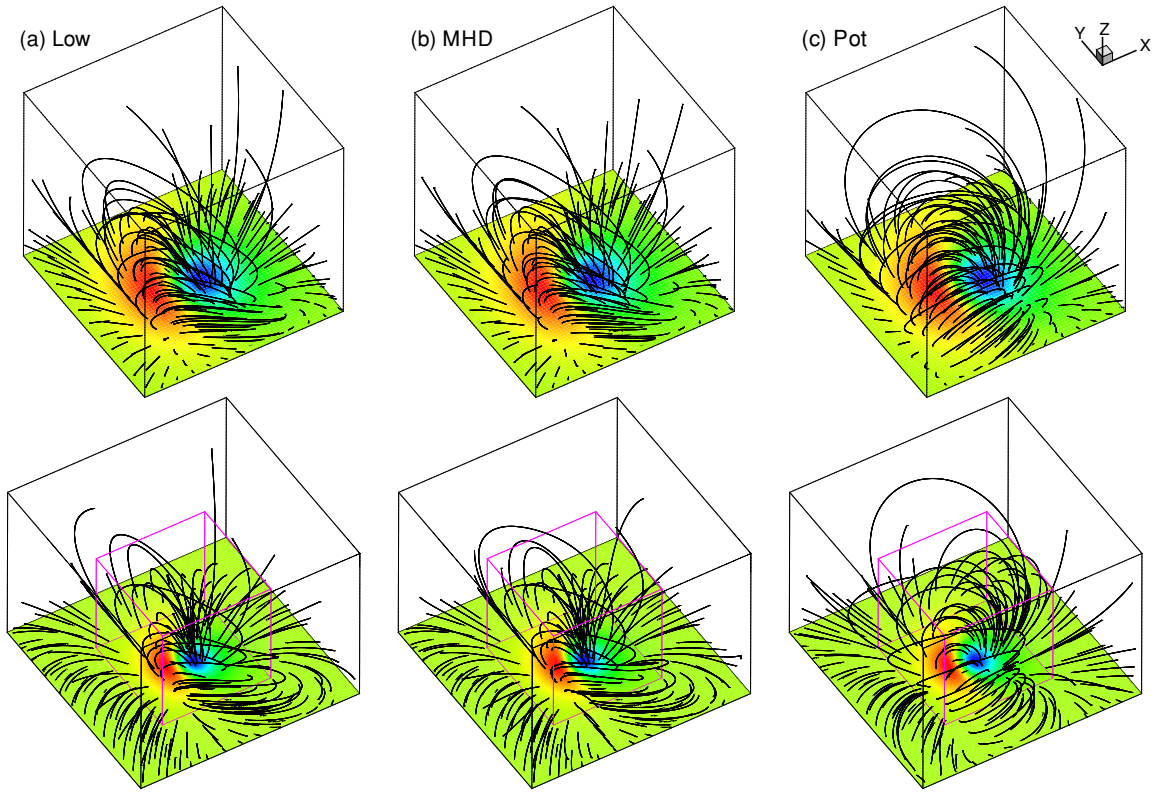

Figure 1. CASE I: magnetic-field lines with a contour of B_z on the bottom surface for Low & Lou's solution (a), the MHD result (b), and the initial potential field (c). The top row enlarges the central region outlined by the small cube in the bottom row.

where n and a are constants. Then, the magnetic field can be derived by

$$B_r = \frac{1}{r^2 \sin\theta}\frac{\partial A}{\partial \theta}, \quad B_\theta = -\frac{1}{r \sin\theta}\frac{\partial A}{\partial r}, \quad B_\phi = \frac{1}{r \sin\theta} Q, \tag{15}$$

where $A = P(\cos\theta)/r^n$ and $Q = aA^{1+1/n}$. The solution P of Equation (14) is uniquely determined by two eigenvalues, n and its number of nodes m (Low & Lou 1990; Amari et al. 2006). By arbitrarily positioning a plane in the space of the analytical fields, one obtains a different kind of test case, in which the plane represents the bottom-boundary condition for extrapolation of the overlying fields. The position of the plane is characterized by two additional parameters, l and Φ. Here, we choose the solutions of test cases in Schrijver et al. (2006), where six existing methods of NLFFF reconstruction are quantitatively compared by using Low & Lou's model. The solutions are given by $n = 1$, $m = 1$, $l = 0.3$, and $\Phi = \pi/4$ (CASE I); and $n = 3$, $m = 1$, $l = 0.3$, and $\Phi = 4\pi/5$(CASE II), respectively. The same test solutions were also used in several studies on different computational methods for the NLFFF (Wheatland et al. 2000; Amari et al. 2006; Valori et al. 2007; He & Wang 2008). In this section, a detailed analysis of the modeling of CASE I is presented, and the results of CASE II are simply reported afterward.

The computational domain is $x, y \in [-1, +1]$ and $z \in [0, 2]$ for both cases. The numerical value of the field is properly scaled such that the central domain of volume (i.e., $x, y \in [-0.5, +0.5]$ and $z \in [0, 1]$) has low plasma $\beta \leqslant 10^{-2}$. Obviously, even after reaching an exact magnetohydrostatic state of $\mathbf{v} = \mathbf{0}$ in our simulation, the magnetic field cannot be exactly force free because of finite β in the full MHD modeling. Thus, in theory, for the central region with the strong field, relative error between the full MHD result and the exact force-free-field solution is on the order of 10^{-2}, while for the full volume it will be larger because of a higher β.

In the present run, for the first $10\tau_A$ (Alfvén time), the field in the volume is driven by the bottom vector that is linearly changed from the potential field to Low & Lou's solution and then relaxed to a numerical magnetohydrostatic state for the following $50\tau_A$.

CASE I is first performed on a $128 \times 128 \times 100$ non-uniform grid. Figure 1 shows the comparison of the MHD result and Low & Lou's solution. It also shows the potential field used for initializing the computation. The field lines shown are traced from footpoints equally spaced at the bottom surface. In the central region (top row of the figure), the MHD result is highly in agreement with Low & Lou's solution, as can be seen from the high similarity of most of the field lines. The field lines in the entire volume (bottom row of the figure) are also similar but deviate near the top boundary mainly because of the high β condition. Figure 2 further demonstrates the MHD results by plotting the values on a chosen straight line. Note that the profiles of the MHD results and Low & Lou's solution almost coincide in the central region.

For a detailed comparison of quantities, a suite of metrics introduced by Schrijver et al. (2006) is computed. The five metrics compare either local characteristics, including vector magnitudes and directions at each point, or global energy content. They are, respectively, the vector correlation $C_{\rm vec}$:

$$C_{\rm vec} \equiv \sum_i \mathbf{B}_i \cdot \mathbf{b}_i \Big/ \left(\sum_i |\mathbf{B}_i|^2 \sum_i |\mathbf{b}_i|^2 \right), \tag{16}$$

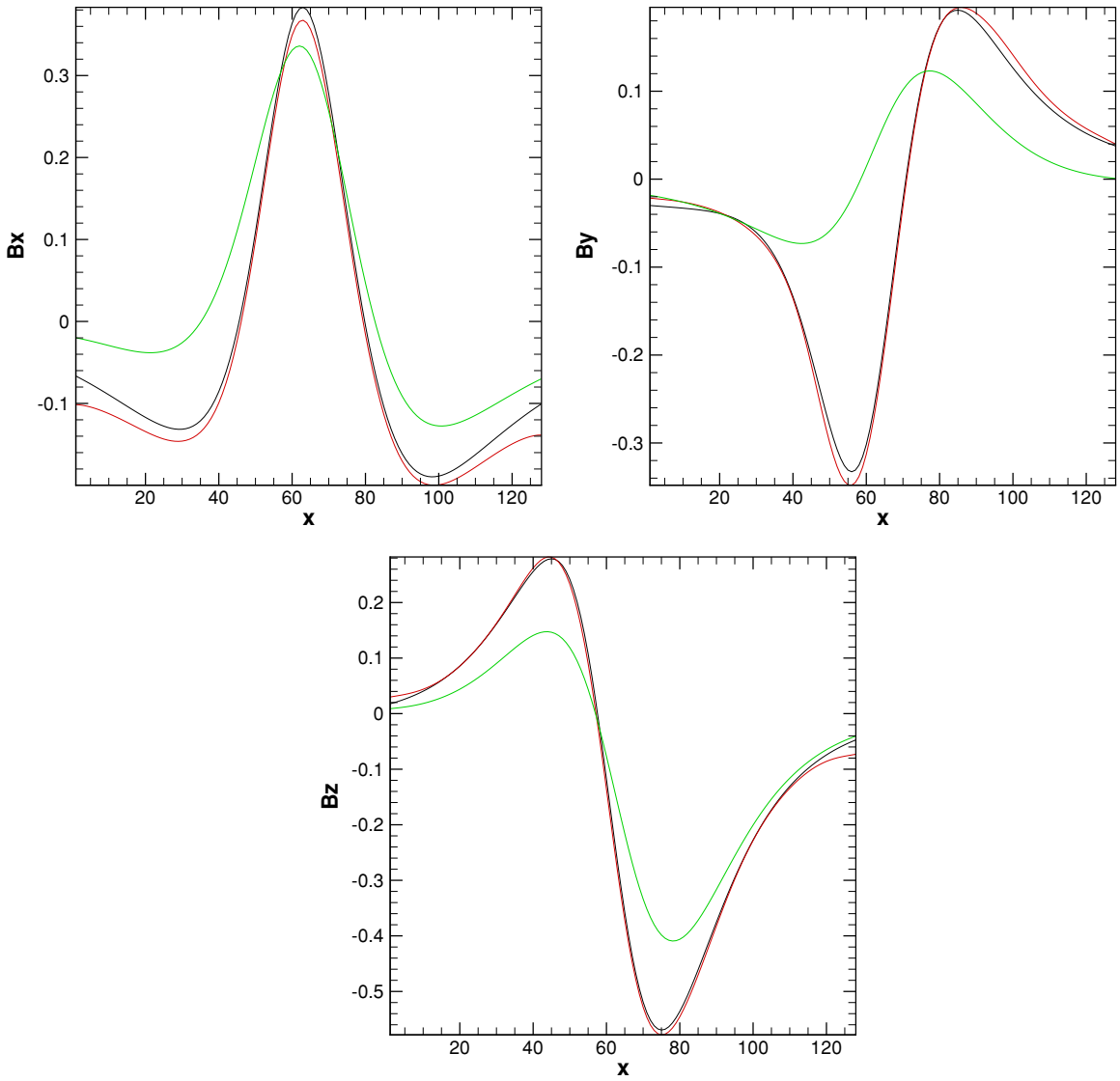

Figure 2. CASE I: B_x, B_y, and B_z along the line of ($y = -0.22, z = 0.31$) or grid point of ($50\Delta y, 20\Delta z$). Black lines denote Low & Lou's solution, red lines stand for the MHD results, and green lines show the potential field.

the metric $C_{\rm CS}$ based on the Cauchy–Schwarz inequality:

$$C_{\rm CS} \equiv \frac{1}{M}\sum_i \frac{\mathbf{B}_i \cdot \mathbf{b}_i}{|\mathbf{B}_i||\mathbf{b}_i|}, \tag{17}$$

the normalized and mean vector error $E'_{\rm n}$, $E'_{\rm m}$:

$$E_{\rm n} \equiv \sum_i |\mathbf{b}_i - \mathbf{B}_i| \Big/ \sum_i |\mathbf{B}_i|, \quad E'_{\rm n} = 1 - E_{\rm n}, \tag{18}$$

$$E_{\rm m} \equiv \frac{1}{M}\sum_i \frac{|\mathbf{B}_i - \mathbf{b}_i|}{|\mathbf{B}_i|}; \quad E'_{\rm m} = 1 - E_{\rm m}, \tag{19}$$

and the normalized total energy of the magnetic field:

$$\epsilon \equiv \frac{\sum_i |\mathbf{b}_i|^2}{\sum_i |\mathbf{B}_i|^2}, \tag{20}$$

where $\mathbf{B}_i$ and $\mathbf{b}_i$ denote Low & Lou's solution and the numerical results, respectively; i denotes the indices of the grid points; and M is the total number of grid points involved. As can be seen, an exact extrapolation will have all the metrics equal unity with such definitions, and the closer to unity it is, the better extrapolation will be, and vice versa. Detailed descriptions for these metrics can be found in Amari et al. (2006), Schrijver et al. (2006), and Valori et al. (2007).

The results are given in Table 2 for both the central region and entire domain. In the central region, the MHD result differs from Low & Lou's solution only on the order of 10^{-3} for the vector directions, and by $\sim$6% for the vector norms, which is consistent with our anticipation because the error is not only caused by the numerical method but also by finite plasma β. The relative error should be reduced if the effect of β is removed. For the same reason, the differences in the entire domain become a bit larger, but the information about the vector directions is well preserved.

We also plot the evolution of the metrics to show the process of the system converging toward the near-force-free state (Figure 3, left). At the first $10\tau_{\rm A}$, all the metrics evolve at fast rates, as the system is driven by the Lorentz force injected from the bottom boundary. Then, after the bottom surface fully matches the magnetogram (of Low & Lou's solution), the system begins to relax and reach a "steady state," with the metrics slowly

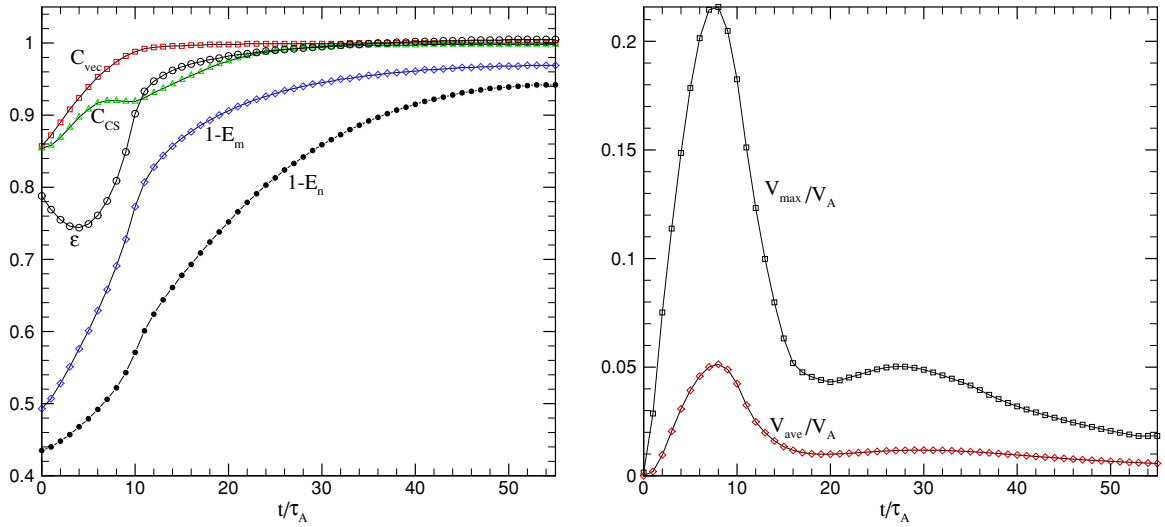

Figure 3. Evolution of the five metrics for the central region (left) and plasma velocity (right) during time from $t = 0$ to $t = 55\tau_A$. Both the maximal velocity v_{max} and average velocity $v_{ave} = \frac{1}{M}\sum_i |\mathbf{v}_i|$ are plotted. Note that the maximal velocity is just about triple the average value at the end time.

Table 2
CASE I: Model Results of the Metrics for the Central Region and Entire Domain

Model	C_{vec}	C_{CS}	E'_n	E'_m	ϵ
For the central region					
Low	1	1	1	1	1
MHD_{128}	1.000	0.998	0.969	0.942	1.005
Potential	0.857	0.854	0.493	0.435	0.788
$Wiegelmann^*_{64}$	1.00	1.00	0.97	0.96	1.02
MHD_{64}	1.00	0.99	0.94	0.89	1.02
$McTiernan^*_{64}$	1.00	0.99	0.94	0.85	1.01
$Valori^*_{64}$	1.00	0.98	0.90	0.87	0.98
For the entire domain					
Low	1	1	1	1	1
MHD_{128}	0.998	0.935	0.886	0.712	1.009
Potential	0.850	0.805	0.443	0.360	0.753
$Wiegelmann^*_{64}$	1.00	1.00	0.98	0.98	1.02
$McTiernan^*_{64}$	1.00	0.99	0.92	0.87	1.00
MHD_{64}	1.00	0.93	0.84	0.65	1.03
$Valori^*_{64}$	0.99	0.68	0.71	0.33	0.98

Notes. Results performed on the $128 \times 128 \times 100$ non-uniform grid are labeled by the subscript 128. The subscript 64 denotes that the calculation is performed on a 64^3 uniform grid, and the superscript $*$ denotes the reported results in Schrijver et al. (2006).

increasing and stagnating at the end of the simulation. This steady state is indeed a static equilibrium, as seen from Figure 3 (right). It shows that the magnitude of the residual velocity of plasma is only several thousandths of the Alfvén speed (v_A) and is on the order of the numerical error $O(\Delta x^2)$ of the CESE method.

To assess the capability to control the error $\nabla \cdot \mathbf{B}$, two additional metrics are presented. One is a simple average of the error in the entire computational volume V,

$$E_{\mathbf{B}} = \frac{1}{V}\sum_V |\nabla \cdot \mathbf{B}| dV. \quad (21)$$

The other is introduced to measure the effect caused by $\nabla \cdot \mathbf{B}$ in the numerical computation. Actually, the nonzero $\nabla \cdot \mathbf{B}$ or the magnetic monopole introduces to the system an unphysical force $\mathbf{F}_{unphysical} = \mathbf{B}\nabla \cdot \mathbf{B}$ parallel to the field line (Dellar 2001). To evaluate the effect of this unphysical force, the ratio of its magnitude to that of the magnetic-pressure force (i.e., the magnetic-pressure gradient) is calculated as

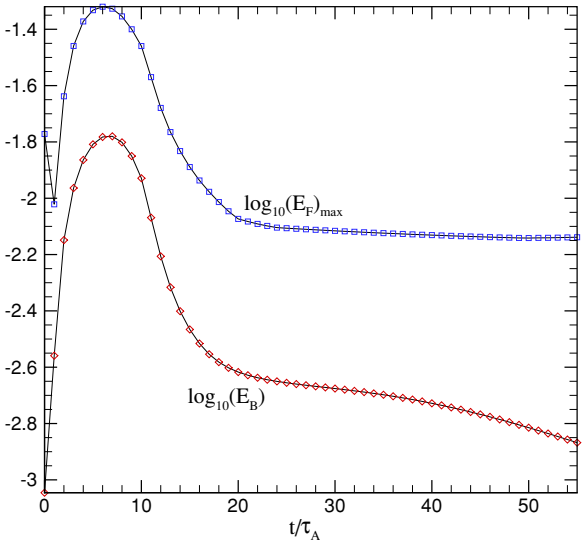

Figure 4. Evolution of the two metrics $E_{\mathbf{B}}$ and $(E_{\mathbf{F}})_{max}$ for $\nabla \cdot \mathbf{B}$.

$$E_{\mathbf{F}} = \frac{|\mathbf{B}\nabla \cdot \mathbf{B}|}{|\nabla(\mathbf{B} \cdot \mathbf{B}/2)|}. \quad (22)$$

Figure 4 shows the evolution of $E_{\mathbf{B}}$ and the maximal $E_{\mathbf{F}}$ in the computational volume. The average error $E_{\mathbf{B}}$ first climbs to a peak of $10^{-1.8} \approx 0.015$ in the system-driven process (from time $t = 0$ to $8\tau_A$), and then quickly drops to the value of only $10^{-2.6} \approx 0.0025$ at $20\tau_A$ and keeps decreasing to the end of the simulation time. A similar variation describes the maximal $E_{\mathbf{F}}$, which is maintained below 0.01during the relaxation process ($t > 15\tau_A$). All this means that the evolution of the magnetic field is affected little by the unphysical force.

For a comparison of the results of the present test and those reported by Schrijver et al. (2006), we also run the simulation of CASE I on the same $64 \times 64 \times 64$ uniform grid as used by Schrijver et al. (2006). Our results and the reported results

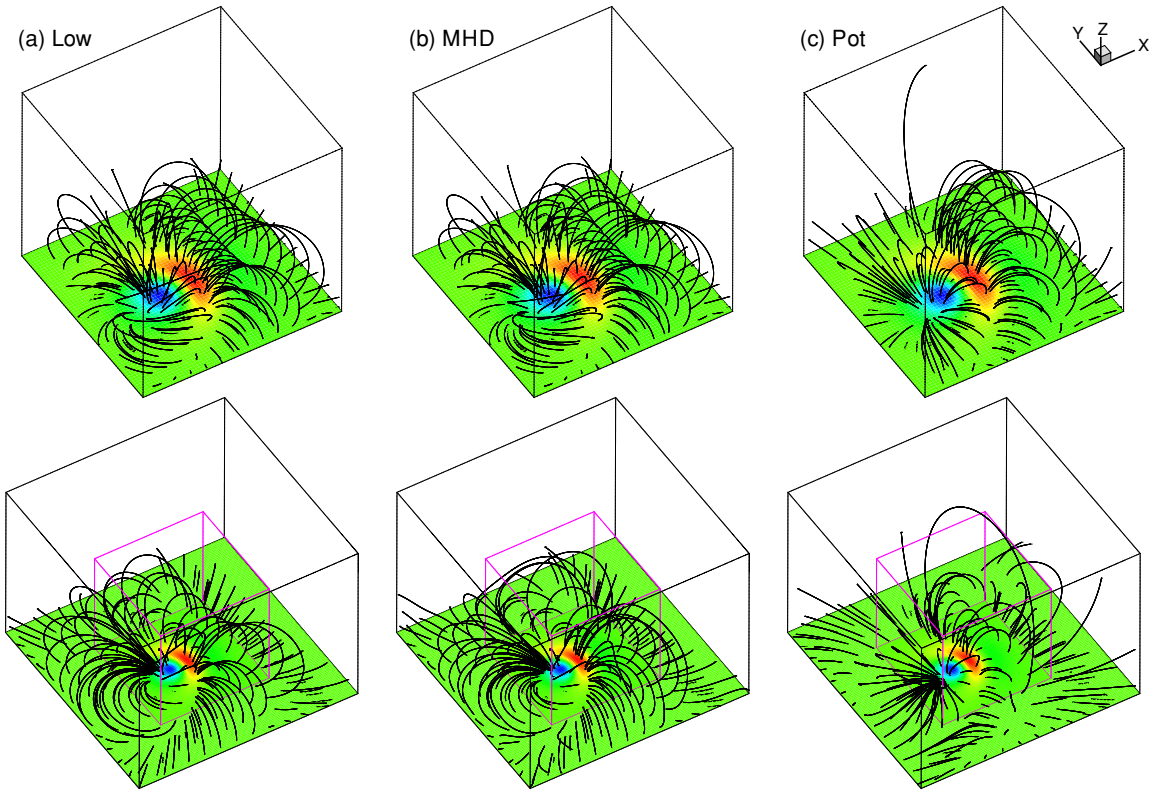

Figure 5. Same as Figure 1, but for CASE II.

in Table 1 of Schrijver et al. (2006) are again presented in Table 2 in order of decreasing quality of agreement. Here, only the first three preferable modeling results reported by Schrijver et al. (2006) are shown, and are calculated using the optimization method with the weighting function from Wiegelmann (2004), the optimization method implemented by McTiernan (Wheatland et al. 2000), and the magnetofrictional method by Valori et al. (2005), respectively. It shows that our MHD results in the central region are close to the "best-fit model" results reported by Wiegelmann and a little better than McTiernan's, but a bit worse for the entire domain because the low β condition is unsatisfied. We note that all the boundaries (including the side and top faces) are provided with Low & Lou's values in their models, while only the lower boundary is specified in our model. It is also worth noting that our results are better than those from the similar MHD-relaxation method used by Valori et al. (2005), especially for the entire domain, which may be due to the implementation of the NRBCs and the more natural way of relaxing the stressed state.

The results (magnetic-field lines and the five metrics) for CASE II on the grid of $128 \times 128 \times 100$ are shown in Figure 5 and Table 3. In this case, the errors for the entire volume are much larger than those for the central region, as shown especially by the most sensitive metric, $E'_{\rm m}$, and the situation is more significant than that of CASE I. That is mainly because the magnetic flux is more concentrated in the interior of the volume, and because the field decreases much faster away from the central region in this case than in CASE I. Then, the corresponding plasma β in the weak-field region will be higher in CASE II than in CASE I using the same scaling for the magnetic field and the same initial pressure configuration. A higher β will introduce a larger error, as we have noted, even though the results are comparable to the best of those reported by Schrijver et al. (2006).

Table 3
CASE II: Model Results of the Metrics for the Central Region and Entire Domain

Model	$C_{\rm vec}$	$C_{\rm CS}$	$E'_{\rm n}$	$E'_{\rm m}$	ϵ
For the central region					
Low	1	1	1	1	1
MHD	0.999	0.967	0.915	0.754	1.005
Potential	0.924	0.674	0.572	0.317	0.888
For the entire domain					
Low	1	1	1	1	1
MHD	0.999	0.706	0.846	0.166	1.005
Potential	0.922	0.396	0.470	−0.262	0.888

4. CONCLUSIONS

In this paper, the approach of MHD relaxation for the NLFFF reconstruction is implemented with the CESE–MHD method. The scheme is conceptually similar to the MHD evolutionary method of Mikić & Linker (1994) and McClymont et al. (1997), which solves the resistive and viscous MHD system to achieve near-force-free equilibrium from an initial state by using the method of stressing and relaxing. Our improvements include: (1) the full MHD system is solved, (2) a modern and high-performance numerical method (CESE) is used, and (3) a simpler but effective boundary condition is adopted.

In detail, to solve the full MHD equations, the effect of gas pressure is taken into consideration by initially giving an isothermal plasma in hydrostatic equilibrium in solar gravitation. This is more realistic because the exact NLFFF does not exist. We face the challenge of modeling the full MHD with an extreme low β using the CESE method, which is based on an existing code we have developed for the time-dependent 3D MHD simulation of problems of the solar–terrestrial system (Feng et al. 2006, 2007, 2010). The bottom-boundary condition, inspired

by the stress-and-relax method, is given by linearly changing the transverse field from the initial potential field to the magnetogram, keeping other quantities fixed. During this process, Lorentz forces are continuously injected to drive the system. For the side and top surfaces, the boundary effects are minimized by the NRBCs based on the projected-characteristics method.

We apply our scheme to reconstruct two well-known, half-analytic NLFFF solutions by Low & Lou for validation, using only the corresponding bottom-vector magnetogram. The same solutions were carried out by most of the present NLFFF methods, and detailed quantities (the metrics) were reported, which makes our quantitative comparison with them possible. Both results of the two cases demonstrate the success of our reconstructions, and they are comparable with the best of those reported by Schrijver et al. (2006), even without removing the error caused by the finite β of the plasma. The evolution of the metrics and velocity over time also demonstrates that the system indeed reaches the static equilibrium, and the value of the residual velocity in the system is only at the level of the numerical discretization error. Furthermore, the well-known but annoying error of $\nabla \cdot \mathbf{B}$ in the numerical MHD is effectively reduced by the combination of the CESE method (with Powell's source), the diffusive control, and the Poisson projection. As shown by our introduced metric for $\nabla \cdot \mathbf{B}$, the effect of this error is only equivalent to exerting on the plasma an unphysical force that is weaker than 1% of the magnetic-pressure force. Finally, no negative pressure was found in the model after checking solution data after every time step.

In the present reconstructions, the ideal MHD is modeled without the resistive term, because the magnetic topology of the field changes little in evolution. A more complex or general field configuration may require a significant change in topology (Roumeliotis 1996; Valori et al. 2005), which means resistivity is needed for reconnection of the field lines. In our model, this can be readily realized by specifying a proper, nonzero η. Applications to more complex solutions, such as the Titov & Démoulin force-free equilibrium (Titov & Démoulin 1999; Valori et al. 2010), and real solar-vector magnetograms are planned for our next work.

One great challenge of the NLFFF reconstructions is the limitation of computational resources, especially for the extrapolation of currently available high-resolution and large-field-view magnetograms. At present, a promising avenue is parallel computing with the adaptive mesh-refinement (AMR) technique utilized in the grid system. Our code has already been highly parallelized on the share-memory parallel computer by using the message-passing-interface library. By overlapping interprocessor communication with the advancing solution, great scaling (i.e., parallel speedup) of the code on multiprocessors ($\sim$256) has been achieved and can be readily used for application to the large grid ($\geqslant 512^3$). Also, as the CESE–MHD method has been realized on the AMR grid system (AMR–CESE–MHD) with the help of the PARAMESH toolkit (a package for implementation of the AMR technique on existing code (MacNeice et al. 2000), we look forward to a significant reduction in computer resources for reconstruction with the magnetogram of the same size and application to the larger magnetograms by using the AMR–CESE–MHD code. Moreover, we have recently extended the CESE–MHD method on more general curvilinear AMR grids, including a spherical grid that can represent the photosphere more precisely than the rectangular grid (Jiang et al. 2010). This implementation paves the way for the NLFFF reconstruction in the spherical-geometry grid, and our future task is to work on the global-field extrapolation with the full disk-vector magnetogram available on SDO/HMI.

The work is jointly supported by the National Natural Science Foundation of China (41031066, 40921063, 40874091, 40890162, 41074122, and 40536029), the 973 project under grant 2006CB806304, and the Specialized Research Fund for State Key Laboratories.

APPENDIX A

IMPLEMENTATION OF THE PROJECTED-CHARACTERISTICS METHOD

To derive the method of projected characteristics, we write the full 3D MHD equations in the vector-matrix form that is convenient for eigendecomposition,

$$\frac{\partial \mathbf{W}}{\partial t} = -A\frac{\partial \mathbf{W}}{\partial x} - B\frac{\partial \mathbf{W}}{\partial y} - C\frac{\partial \mathbf{W}}{\partial z} + \mathbf{S}, \tag{A1}$$

where $\mathbf{W}$ represents the primary physical quantities: $\mathbf{W} = (\rho, v_x, v_y, v_z, p, B_x, B_y, B_z)$, and

$$A = \begin{pmatrix} v_x & \rho & 0 & 0 & 0 & 0 & 0 & 0 \\ 0 & v_x & 0 & 0 & 1/\rho & 0 & B_y/\rho & B_z/\rho \\ 0 & 0 & v_x & 0 & 0 & 0 & -B_x/\rho & 0 \\ 0 & 0 & 0 & v_x & 0 & 0 & 0 & -B_x/\rho \\ 0 & \gamma p & 0 & 0 & v_x & 0 & 0 & 0 \\ 0 & 0 & 0 & 0 & 0 & v_x & 0 & 0 \\ 0 & B_y & -B_x & 0 & 0 & 0 & v_x & 0 \\ 0 & B_z & 0 & -B_x & 0 & 0 & 0 & v_x \end{pmatrix}. \tag{A2}$$

$\mathbf{S}$ contains source terms such as gravity and viscosity.

For the boundary faces of the x-direction, the characteristics along the projected normal can be found in the x–t plane. For convenience, Equation (A1) can be written in a more compact form:

$$\frac{\partial \mathbf{W}}{\partial t} = -A\frac{\partial \mathbf{W}}{\partial x} + \mathbf{S}_x, \tag{A3}$$

with $\mathbf{S}_x$ containing all the rest of the parts. By eigendecomposition of matrix A ($A = R\Lambda L$, $L = R^{-1}$), we have eight sets of eigenvalue λ_m and the corresponding left and right eigenvectors $\mathbf{l}_m$, $\mathbf{r}_m$, with $m = 1, 2, 3, \ldots, 8$. Here, Λ is the diagonal matrix whose diagonal elements are the eigenvalues, i.e., $\Lambda_{m,m} = \lambda_m$ and L, R are the square matrices composed by the left and right eigenvectors, respectively. The eight eigenvalues are the entropy wave speed $\lambda_e = v_x$, the magnetic-flux wave speed $\lambda_d = v_x$, a pair of Alfvén wave speeds $\lambda_a^{\pm} = v_x \pm v_a$, and two pairs of magneto-acoustic wave speeds $\lambda_{f,s}^{\pm} = v_x \pm v_{f,s}$, where v_a is the Alfvén speed and $v_{f,s}$ are the magneto-acoustic speeds. The properly scaled right and left eigenvectors corresponding to each eigenvalue are given in Appendix B.

Multiplying Equation (A3) by the left eigenvectors $\mathbf{l}_m$ gives a set of projected normal-characteristic equations (i.e., compatibility equations)

$$\mathbf{l}_m\frac{\partial \mathbf{W}}{\partial t} = -\lambda_m \mathbf{l}_m\frac{\partial \mathbf{W}}{\partial x} + \mathbf{l}_m\mathbf{S}_x \tag{A4}$$

that describes each wave mode by the wave speed of λ_m and the wave amplitude of $\mathbf{l}_m\mathbf{W}$.

In the case of the left boundary in the x-direction, for instance, the projected-characteristic method states that the compatibility

equation must be used when updating the boundary variables if the corresponding eigenvalue is negative (i.e., the outgoing wave). For positive eigenvalues, the nonreflecting conditions need the right-hand side of Equation (A4) to be zero to keep the incoming waves unchanged. Then for practical use, Equation (A4) can be written as

$$\mathbf{l}_m \frac{\partial \mathbf{W}}{\partial t} = \mathrm{RHS}_m \tag{A5}$$

with

$$\mathrm{RHS}_m = \begin{cases} -\lambda_m \mathbf{l}_m \frac{\partial \mathbf{W}}{\partial x} + \mathbf{l}_m \mathbf{S}_x & \lambda_m < 0, \\ 0 & \lambda_m \geqslant 0. \end{cases} \tag{A6}$$

Upwind differences in the normal direction (x-direction here) and Jacobian matrix-splitting method in the tangential direction are used to discretize Equation (A6) when needed,

$$\begin{aligned} \frac{\partial \mathbf{W}}{\partial x} &= \frac{\mathbf{W}^n_{1,j,k} - \mathbf{W}^n_{0,j,k}}{\Delta x}, \\ \mathbf{S}_x &= \mathbf{S} - \frac{1}{\Delta y}\left[B^-\left(\mathbf{W}^n_{0,j+1,k} - \mathbf{W}^n_{0,j,k}\right)\right. \\ &\quad \left. - B^+\left(\mathbf{W}^n_{0,j,k} - \mathbf{W}^n_{0,j-1,k}\right)\right] \\ &\quad - \frac{1}{\Delta z}\left[C^-\left(\mathbf{W}^n_{0,j,k+1} - \mathbf{W}^n_{0,j,k}\right)\right. \\ &\quad \left. - C^+\left(\mathbf{W}^n_{0,j,k} - \mathbf{W}^n_{0,j,k-1}\right)\right], \end{aligned} \tag{A7}$$

where (i, j, k) is the index for grid points and $i = 0$ denotes the left x boundary, while (j, k) visits all mesh points of the boundary surface. Here, B^+, B^- are the positive and negative parts of matrix B, which can be derived by eigendecomposition of matrix $B = R_B \Lambda_B L_B$:

$$B^+ = R_B \frac{\Lambda_B + |\Lambda_B|}{2} L_B, \quad B^- = R_B \frac{\Lambda_B - |\Lambda_B|}{2} L_B. \tag{A8}$$

The matrices C^+ and C^- are defined in the same way. The reason why we use such types of tangential difference is the consideration of numerical stability, as the simple central difference will introduce instability, which we have encountered in practice.

After that, the temporal variations $\frac{\partial \mathbf{W}}{\partial t}$ can be solved by left-multiplying the full set of Equation (A5):

$$L \frac{\partial \mathbf{W}}{\partial t} = \mathbf{RHS} \tag{A9}$$

by eigenvector matrix R of matrix A :

$$\frac{\partial \mathbf{W}}{\partial t} = R(\mathbf{RHS}), \tag{A10}$$

and the advanced variables on the boundary are obtained. In this way, the advancing-variables formulae are very compact and neat and ready for coding. The formulae for the other boundaries can be derived similarly.

APPENDIX B

THE EIGEN SYSTEM OF MATRIX A

$\lambda_e = u$

$$\begin{aligned} \mathbf{r}_e &= (1, 0, 0, 0, 0, 0, 0, 0)^T, \\ \mathbf{l}_e &= (1, 0, 0, 0, -1/a^2, 0, 0, 0); \end{aligned} \tag{B1}$$

$\lambda_d = u$

$$\begin{aligned} \mathbf{r}_d &= (0, 0, 0, 0, 0, 1, 0, 0)^T, \\ \mathbf{l}_d &= (0, 0, 0, 0, 0, 1, 0, 0); \end{aligned} \tag{B2}$$

$\lambda_a^{\pm} = u \pm v_a$

$$\begin{aligned} \mathbf{r}_a^{\pm} &= \left(0, 0, \pm\frac{\beta_z}{\sqrt{2}}, \mp\frac{\beta_y}{\sqrt{2}}, 0, 0, -\sqrt{\frac{\rho}{2}}\beta_z \mathrm{sgn}B_x, \sqrt{\frac{\rho}{2}}\beta_y \mathrm{sgn}B_x\right)^T, \\ \mathbf{l}_a^{\pm} &= \left(0, 0, \pm\frac{\beta_z}{\sqrt{2}}, \mp\frac{\beta_y}{\sqrt{2}}, 0, 0, -\frac{\beta_z}{\sqrt{2\rho}}\mathrm{sgn}B_x, \frac{\beta_y}{\sqrt{2\rho}}\mathrm{sgn}B_x\right); \end{aligned} \tag{B3}$$

$\lambda_f^{\pm} = u \pm v_f$

$$\mathbf{r}_f^{\pm} = \begin{bmatrix} \rho\alpha_f \\ \pm\alpha_f v_f \\ \mp\alpha_s v_s \beta_y \mathrm{sgn}B_x \\ \mp\alpha_s v_s \beta_z \mathrm{sgn}B_x \\ \alpha_f \gamma p \\ 0 \\ \alpha_s \sqrt{\rho} a \beta_y \\ \alpha_s \sqrt{\rho} a \beta_z \end{bmatrix}, \mathbf{l}_f^{\pm} = \begin{bmatrix} 0 \\ \pm\frac{\alpha_f v_f}{2a^2} \\ \mp\frac{\alpha_s}{2a^2} v_s \beta_y \mathrm{sgn}B_x \\ \mp\frac{\alpha_s}{2a^2} v_s \beta_z \mathrm{sgn}B_x \\ \frac{\alpha_f}{2\rho a^2} \\ 0 \\ \frac{\alpha_s}{2\sqrt{\rho}a}\beta_y \\ \frac{\alpha_s}{2\sqrt{\rho}a}\beta_z \end{bmatrix}^T; \tag{B4}$$

$\lambda_s^{\pm} = u \pm v_s$

$$\mathbf{r}_s^{\pm} = \begin{bmatrix} \rho\alpha_s \\ \pm\alpha_s v_s \\ \pm\alpha_f v_f \beta_y \mathrm{sgn}B_x \\ \pm\alpha_f v_f \beta_z \mathrm{sgn}B_x \\ \alpha_s \gamma p \\ 0 \\ -\alpha_f \sqrt{\rho} a \beta_y \\ -\alpha_f \sqrt{\rho} a \beta_z \end{bmatrix}, \mathbf{l}_s^{\pm} = \begin{bmatrix} 0 \\ \pm\frac{\alpha_s v_s}{2a^2} \\ \pm\frac{\alpha_f}{2a^2} v_f \beta_y \mathrm{sgn}B_x \\ \pm\frac{\alpha_f}{2a^2} v_f \beta_z \mathrm{sgn}B_x \\ \frac{\alpha_s}{2\rho a^2} \\ 0 \\ -\frac{\alpha_f}{2\sqrt{\rho}a}\beta_y \\ -\frac{\alpha_f}{2\sqrt{\rho}a}\beta_z \end{bmatrix}^T, \tag{B5}$$

where the Alfvén speed is $v_a = |B_x|/\sqrt{\rho}$ and magneto-acoustic speeds are given by

$$v_{f,s} = \sqrt{\frac{1}{2}\left(\frac{\gamma p + \mathbf{B}\cdot\mathbf{B}}{\rho} \pm \sqrt{\left(\frac{\gamma p + \mathbf{B}\cdot\mathbf{B}}{\rho}\right)^2 - 4\frac{\gamma p B_x^2}{\rho^2}}\right)}. \tag{B6}$$

The auxiliary variables are defined as

$$a = \sqrt{\frac{\gamma p}{\rho}}; \quad \alpha_f^2 = \frac{a^2 - c_s^2}{c_f^2 - c_s^2}; \quad \alpha_s^2 = \frac{c_f^2 - a^2}{c_f^2 - c_s^2},$$

$$\beta_y = \frac{B_y}{\sqrt{B_y^2 + B_z^2}}; \quad \beta_z = \frac{B_z}{\sqrt{B_y^2 + B_z^2}},$$

and when $B_y^2 + B_z^2 = 0$, $\beta_y = \beta_z = 1/\sqrt{2}$.

REFERENCES

Amari, T., Boulmezaoud, T. Z., & Aly, J. J. 2006, A&A, 446, 691
Amari, T., Luciani, J. F., Aly, J. J., Mikić, Z., & Linker, J. 2003, ApJ, 585, 1073
Balsara, D. S., & Spicer, D. 1999, J. Comput. Phys., 148, 133
Dedner, A., Kemm, F., Kröner, D., Munz, C., Schnitzer, T., & Wesenberg, M. 2002, J. Comput. Phys., 175, 645
Dellar, P. J. 2001, J. Comput. Phys., 172, 392
Feng, X. S., Hu, Y., & Wei, F. 2006, Sol. Phys., 235, 235
Feng, X. S., Yang, L. P., Xiang, C. Q., Wu, S. T., Zhou, Y. F., & Zhong, D. K. 2010, ApJ, 723, 300
Feng, X. S., Zhang, Y., Yang, L. P., Wu, S. T., & Dryer, M. 2009, J. Geophys. Res., 114, 10103
Feng, X. S., Zhou, Y., & Wu, S. T. 2007, ApJ, 655, 1110
Hayashi, K. 2005, ApJS, 161, 480
Hayashi, K., Benevolenskaya, E., Hoeksema, T., Liu, Y., & Zhao, X. P. 2006, ApJ, 636, L165
Hayashi, K., Zhao, X. P., & Liu, Y. 2008, J. Geophys. Res., 113, 7104
He, H., & Wang, H. 2008, J. Geophys. Res., 113, 5
Hedstrom, G. W. 1979, J. Comput. Phys., 30, 222
Hu, Y. Q., Feng, X. S., Wu, S. T., & Song, W. B. 2008, J. Geophys. Res., 113, 3106
Jiang, C. W., Feng, X. S., Zhang, J., & Zhong, D. K. 2010, Sol. Phys., 267, 463
Low, B. C., & Lou, Y. Q. 1990, ApJ, 352, 343
MacNeice, P., Olson, K. M., Mobarry, C., de Fainchtein, R., & Packer, C. 2000, Comput. Phys. Commun., 126, 330
Marder, B. 1987, J. Comput. Phys., 68, 48
McClymont, A. N., Jiao, L., & Mikić, Z. 1997, Sol. Phys., 174, 191
McClymont, A. N., & Mikić, Z. 1994, ApJ, 422, 899
Metcalf, T. R., Jiao, L., McClymont, A. N., Canfield, R. C., & Uitenbroek, H. 1995, ApJ, 439, 474
Mikić, Z., & Linker, J. A. 1994, ApJ, 430, 898
Mikić, Z., Linker, J. A., Schnack, D. D., Lionello, R., & Tarditi, A. 1999, Phys. Plasmas, 6, 2217
Mikic, Z., & McClymont, A. N. 1994, in ASP Conf. Ser. 68, Solar Active Region Evolution: Comparing Models with Observations, ed. K. S. Balasubramaniam & G. W. Simon (San Francisco, CA: ASP), 225
Nakagawa, Y. 1981, ApJ, 247, 707
Powell, K. G., Roe, P. L., Linde, T. J., Gombosi, T. I., & de Zeeuw, D. L. 1999, J. Comput. Phys., 154, 284
Priest, E. R., & Forbes, T. G. 2002, A&AR, 10, 313
Régnier, S., Amari, T., & Kersalé, E. 2002, A&A, 392, 1119
Roumeliotis, G. 1996, ApJ, 473, 1095
Schrijver, C. J., et al. 2006, Sol. Phys., 235, 161
Thompson, K. W. 1987, J. Comput. Phys., 68, 1
Titov, V. S., & Démoulin, P. 1999, A&A, 351, 707
Tóth, G. 1996, ApL&C, 34, 245
Tóth, G. 2000, J. Comput. Phys., 161, 605
Tóth, G., de Zeeuw, D. L., Gombosi, T. I., & Powell, K. G. 2006, J. Comput. Phys., 217, 722
Valori, G., Kliem, B., & Fuhrmann, M. 2007, Sol. Phys., 245, 263
Valori, G., Kliem, B., & Keppens, R. 2005, A&A, 433, 335
Valori, G., Kliem, B., Török, T., & Titov, V. S. 2010, A&A, 519, A44
Van der Vorst, H. 1992, SIAM J. Sci. Stat. Comput., 13, 631
Wheatland, M. S., Sturrock, P. A., & Roumeliotis, G. 2000, ApJ, 540, 1150
Wiegelmann, T. 2004, Sol. Phys., 219, 87
Wiegelmann, T. 2008, J. Geophys. Res., 113, 3
Wu, S. T., Wang, A. H., Gary, G. A., Kucera, A., Rybak, J., Liu, Y., Vršnak, B., & Yurchyshyn, V. 2009, Adv. Space Res., 44, 46
Wu, S. T., Wang, A. H., Liu, Y., & Hoeksema, J. T. 2006, ApJ, 652, 800
Wu, S. T., & Wang, J. F. 1987, Comput. Methods Appl. Mech. Eng., 64, 267
Wu, S. T., Zheng, H., Wang, S., Thompson, B. J., Plunkett, S. P., Zhao, X. P., & Dryer, M. 2001, J. Geophys. Res., 106, 25089
Yan, Y., & Li, Z. 2006, ApJ, 638, 1162
Yan, Y., & Sakurai, T. 2000, Sol. Phys., 195, 89
Yang, W. H., Sturrock, P. A., & Antiochos, S. K. 1986, ApJ, 309, 383
Zhang, M., John Yu, S.-T., Henry Lin, S.-C., Chang, S.-C., & Blankson, I. 2006, J. Comput. Phys., 214, 599